1

Nanotechnology-based Materials and Their Interaction with Light

Chapter 1 will be dedicated to nanotechnology-based materials for ultrafast microwave applications and the interactions of these materials mainly semiconducting with light. It will focus on two aspects, the first aspect is to give some trends in new semiconductor materials from three dimensional (3D) to zero dimensional (0D) and the second aspect is to give a deep analysis of the interactions at nanoscale between light and these new materials around photoconductivity and plasmonics. Materials concerned are carbon-based materials (especially graphene and carbon nanotubes), nanowire-based technologies: Si, III-V semiconductors, ZnO, nanostructured materials and metamaterials.

1.1. Review of main trends in 3D to 0D materials

1.1.1. *Main trends in 3D materials for radio frequency (RF) electronics and photonics*

Controlling the permittivity and permeability of three-dimensional (3D) materials appears as a major challenge for future electromagnetism systems. Nanomaterials are high-potential candidates for applications in microwave, millimeter wave, terahertz (THz) and optical systems. During the last decade, numerous research activities have been devoted to the study of artificial materials, such as metamaterials [ENG 06]. Mixing components at the nanoscale results in materials providing superior properties compared with conventional microscale composites and, at the same time, that can be synthesized using simple and inexpensive techniques.

In particular, major research advances have been obtained by the group of Nader Engheta, who worked on specific materials such as epsilon-near-zero (ENZ), mu-near-zero (MNZ), zero-index metamaterials and double-negative materials [ALU 07].

The introduction on the structure of the split-ring resonator (SRR) by J. Pendry in 1999 opened the way for the demonstration of metamaterials based on the periodic implantation of such SRRs [PEN 99, PEN 07, SMI 00]. The implementation of the first effective medium with left-handed properties by D.R. Smith in 2000 was possible due to the use of small metallic resonators, SRRs. The SRR appeared as the first non-magnetic resonator capable of showing negative values of the magnetic permeability around its resonance frequency.

The control and the tunability of those materials remain as the great future challenges in this field.

1.1.2. *Main trends in 2D materials for RF electronics and photonics*

The combination of the unique properties of two-dimensional (2D) semiconductor materials, such as graphene, with new device concepts and nanotechnology can overcome some of the main limitations of traditional electronics in terms of maximum operating frequency, linearity and power dissipation.

1.1.2.1. *The example of graphene*

Graphene is a flat monolayer of carbon atoms forming a 2D honeycomb lattice. Graphene is a basic building block of graphite and carbon nanotubes (CNTs). Graphene properties were first introduced by Wallace in 1947.

At the beginning of the 21st Century, Andre Geim, Konstantin Novoselov and their collaborators from the University of Manchester (UK), and the Institute for Microelectronics Technology in Chernogolovka (Russia), published their results on graphene structures in October 2004 [NOV 04].

After reviewing some important papers in the literature devoted to this new material, we can derive some basic characteristics of graphene materials and their main applications.

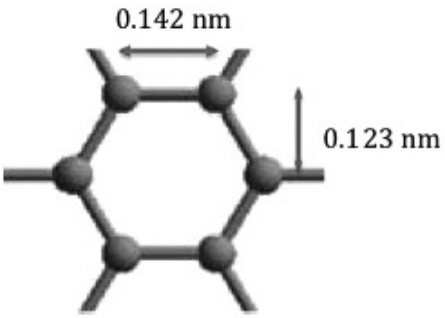

Figure 1.1. *Graphene: a flat monolayer of carbon atoms for ming a 2D honeycomb lattice*

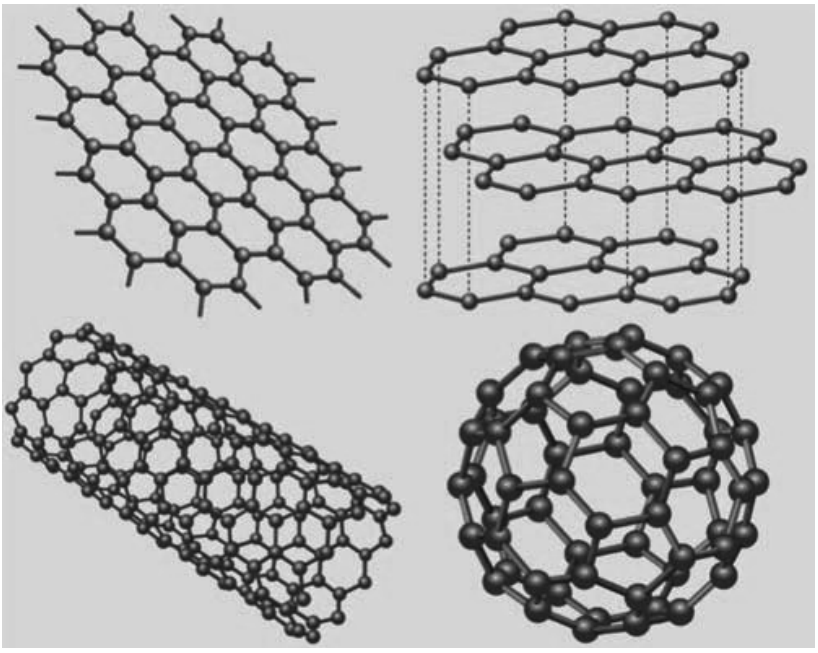

Figure 1.2. *Top left: graphene is a honeycomb lattice of carbon atoms. Top right: graphite can be viewed as a stack of graphene layers. Bottom left: carbon nanotubes are rolled-up cylinders of graphene. Bottom right: fullerenes C60 are molecules consisting of wrapped graphene by the introduction of pentagons on the hexagonal lattice [CAS 06]*

Parameters	Typical characteristics
Thickness	0.142 nm
Band structure	Semi-metal or zero-bandgap semiconductor
Electron transport	Ballistic at room temperature Relativistic quantum Dirac equation
Carrier mobilities	1,00,000 cm²/V.s in suspended graphene 10,000 cm²/V.s in graphene on substrate
Young's modulus	1.5 TPa
Breakdown current	10^8 A/cm²
Current density	1 A/μm
Transistor cutoff frequency	350 GHz
Carrier density	10^{14} cm^{-2}
Optical absorption	$\pi\alpha$~2.3%
Thermal conductivity	5,000 W/m.K

Table 1.1. *Typical characteristics of graphene [CAS 09, AVO 10, WAN 10, LOV 12, WU 12, SCH 10]*

One of the main characteristics of this material is that intrinsic graphene is a semi-metal or a zero-bandgap semiconductor. In this material, the electron transport is ballistic at room temperature and is described by a relativistic-like quantum Dirac equation instead of a Schrödinger equation.

Graphene demonstrates not only an electric field effect but also a ballistic electronic transport, which results in very high charge carrier mobilities more than 100,000 cm²/V.s.

Such mobilities of graphene exceed that of silicon by at least a factor of 40, which makes it particularly important for designers of the next-generation fast transistors.

Also, graphene has a Young's modulus of 1.5 TPa.

Due to these unique properties, graphene is very promising for high-frequency nanoelectronic devices, such as oscillators and switches. In practical applications, graphene is deposited on a SiO_2 layer with a typical thickness of 300 nm, which is grown over a doped silicon substrate.

It is interesting to note that the conductivity of the graphene sheet is an anisotropic tensor and it can be controlled by applying an electrostatic and magnetostatic biasing field. This property introduces the possibility of developing new applications, which cannot be obtained by conventional conducting materials of fixed conductivities.

1.1.2.2. *Graphene for RF applications*

Recent results on the use of graphene for microwave applications enabled us to review some functions covering the field of nanocircuits up to the realization of new microwave functions based on this material; among those, we will review the following functions in Chapter 2: RF mixers, frequency multipliers, antennas, isolator, circuits, transistors and field-effect transistors (FETs), photodetectors, barristor, optoelectronic functions such as graphene photodetector and other potential applications of graphene, superconducting FETs and room-temperature spintronics, and transparent electrodes [OBE 11].

Some helpful analysis on the use of graphene for microwave applications will be given in Chapter 3.

1.1.3. *Review of other two-dimensional structures for RF electronic applications*

1.1.3.1. *Plasmonic structures*

Plasmonics is based on the interaction process between an electromagnetic radiation and the conduction electrons at metallic interfaces or in small metallic nanostructures. For noble metals such as Ag and Au, the plasma frequency is in the visible or ultraviolet region; therefore, their permittivity has negative real parts in the optical frequencies. These metals behave as plasmonic materials, and their interaction with optical signals involves surface plasmon resonances (SPRs). These plasmonic structures provide interesting possibilities not only for synthesizing subwavelength cavities or new metamaterials at infrared and optical frequencies, but also for addressing new microwave functions involving confined optical interactions and microwave modulation of the electric field at a semiconductor/dielectric interface [AHM 12].

A detailed approach of plasmonic structures has been given in the Introduction.

1.1.3.2. *Two-dimensional semiconductor materials*

The 2D semiconductors such as transition metal dichalcogenides (such as MoS_2, $MoSe_2$, WS_2 or WSe_2) show excellent device characteristics, as well as novel optical, electrical and optoelectronic characteristics due to quantum size effects. Recent research of 2D materials based on chalcogenides and/or III–V semiconductors on Si/SiO_2 substrates has been achieved. It is important for both fundamental science and applications, such as electronics, photonics and chemical sensing. Unlike the zero-bandgap graphene, it is possible to tune the bandgap of 2D semiconductor materials by the choice of elements and the number of layers. The large bandgaps of 2D semiconductors (e.g. 1.8 eV for MoS_2 monolayer nanosheet) and their carrier mobility make these materials very attractive for the next-generation nanoelectronic and nanophotonic devices [JAV 13].

1.1.4. *Main trends in 1D materials for RF electronics and photonics*

This section deals with recent research on carbon-based and non-carbon-based one-dimensional (1D) materials such as nanorods/carbon nanotubes (CNTs), boron nitride nanotubes (BNNTs) and semiconductor nanowires (NWs).

1.1.4.1. *CNT materials and microwave applications*

It is well known that CNTs are cylinders of nanometer (nm) diameter of a graphene sheet wrapped up to form a tube. Since their experimental discovery in 1991 [IIJ 91], numerous research efforts have been devoted to exploring their physical properties including electromagnetic wave interaction of the conducting CNTs, which seems to contain important features compared with traditional conductors [GHA 11].

Single-wall carbon nanotubes (SWCNTs) can be seen as rolled-up sheets of graphene, i.e. a monolayer hexagonal lattice of carbon atoms. They can be uniquely described by a double index or chiral vector (n,m) that corresponds to the way the graphene sheet is rolled up, i.e. the angle it makes with the vectors of the lattice and how tightly the CNT is rolled up. According to this index, an SWCNT may be metallic (i.e. no bandgap) or semiconducting (i.e. diameter-dependent bandgap). The only truly metallic CNTs are the

armchair n = m, rolled along vector a_2 as shown in Figure 1.3. For zigzag (rolled along vector a_1) and chiral SWCNTs, there are two cases: if n − m = 3j + 1 or 3j + 2, then the CNTs are semiconducting. However, if n − m = 3j, the bandgap is sufficiently small in that they behave as metals at ambient temperature. They are semi-metallic tubes, usually referred to as being simply metallic CNTs. In this case, from Figure 1.3, or the three-congruence, it is simple to conclude that, if all chiral vectors have the same probability, there should be 1/3 metallic SWCNTs and 2/3 semiconducting. Common CNT production methods usually have a narrow diameter distribution but chiral vectors of semiconductor and metal SWCNTs are equivalently distributed.

Multiwall carbon nanotubes (MWCNTs) are concentric shells like Russian dolls made up of SWCNTs. They are available in a variety of diameters, number of shells, etc.

CNTs can display huge length-to-diameter aspect ratios because the diameter varies from 1 nm to a few tens of nm, but lengths up to half a meter have been reported [CHA 08]. Usual lengths vary from less than 1µm to 100 µm depending on the fabrication technique and application.

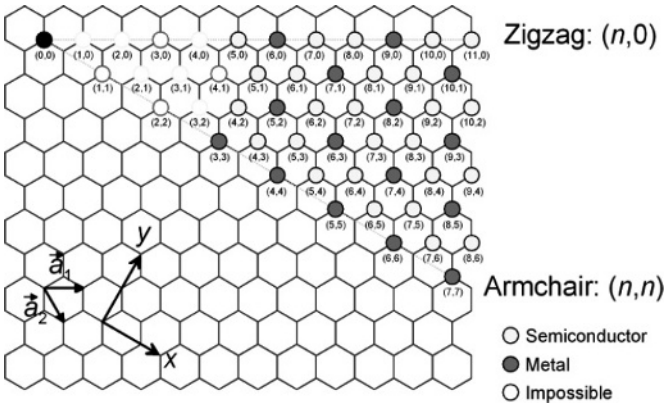

Figure 1.3. *Chiral vector of CNT*

The earliest research has been focused on the synthesis of CNTs necessary for experiments. The progress of common growth techniques including arc discharge and laser ablation of graphite pieces and later chemical vapor deposition (CVD) and plasma-enhanced CVD has

significantly improved the quality of the CNTs [MEY 05]. Recently, many companies have concentrated their efforts to develop and control the growth techniques to perform very high purity and uniform CNTs in length and diameter. The physical properties of CNTs [SAI 98] have demonstrated unique electronic structure depending on their dimensions and chiralities, which have been considered as a major discovery in the field of semiconductor devices. In addition, due to strong covalent carbon–carbon bonding, CNTs present very high tensile strength, thermal and electrical conductivity. Hence, those mechanical and electrical properties make them also very attractive for reinforcing composite materials for aerospace applications. Usually, CNTs are classified into two categories: SWCNTs that are composed of a single graphitic cylinder, where the diameter varies from 0.7 to 2 nm, and MWCNTs that are composed of several concentric graphitic layers, where the diameter varies from 10 to 200 nm. Commercial CNTs are available in a powder form where they are entangled and randomly distributed [ZHA 13].

1.1.4.1.1 Carbon nanotubes for RF applications

CNTs are competitive elements in many RF applications like high-frequency transistors, AM demodulators, matched loads, transmission lines and antennas.

The knowledge of dielectric properties at low frequency (direct current (DC) to 1 MHz) as well as high frequency (above 1 MHz) is the key for developing novel electronic devices such as radio frequency-miniaturized resonators [SAB 09a, SAB 09b] as electronic model for future implementation [SAB 09c]. Therefore, the electrical characterization at radio frequency/microwave (RF/M) bands becomes a challenge where common measurement techniques are inappropriate. For high-frequency measurements, complex permittivity is usually used to describe the dielectric properties of a material where the real part of the permittivity is related to the dielectric constant and the imaginary part can be associated with the conductivity [TRI 14].

1.1.4.2. *BNNT materials and microwave applications*

Theoretically predicted in 1994, BNNTs appeared as a 1D allotrope of a 2D sheet of boron nitride in a hexagonal lattice with alternating boron and nitride atoms [RUB 94, COH 10].

Similar to the CNTs, BNNTs have many unique properties. In particular, BNNTs are semiconductors with a wide bandgap (~5.5 eV) weakly dependent on the tube diameter, helicity and the number of walls. Compared with the CNTs, BNNTs have not only high thermal conductivity but also high oxidation resistivity, as well as high thermal and chemical stability, which render BNNTs a promising tubular material for developing nanotube-based electronic devices in certain hazardous and high-temperature environments [WAN 09, WAN 10].

1.1.5. *Other 1D materials for RF applications*

Semiconductor NWs have drawn enormous research efforts for their special material properties and wide-ranging device applications with outstanding performances [SAB 09c, TRI 11, RUB 04]. As one of the elementary building blocks of nanoelectronic devices, NWs configured as FETs have been shown to operate at ultralow power below microwatts with an enhanced operational speed. Semiconductor NWs, such as groups IV [QIN 08, HOC 08], III–V [CHA 08, CUI 03] and II–VI [XIA 06, BRY 06], and others [NIL 08, LIU 05, COM 05] have demonstrated the prospective construction of state-of-the-art devices.

This section deals with recent research on non-carbon-based 1D materials such as semiconductor NWs.

1.1.5.1. *Semiconductor nanowires Si and II–V compounds*

Semiconductor NWs have been extensively investigated as nanoscale building blocks for novel nanoelectronics and nanophotonics. Both top-down fabrications based on conventional microfabrication technologies and top-down fabrication based on chemical synthesis (from the gaseous or from the liquid phase) are possible. In addition to being driven by the need to overcome some limitations of the top-down fabrication, the study of bottom-up NW growth is motivated by their interesting electrical transport and optical properties that are remarkably different from those of the corresponding bulk materials. Homogeneous NWs can be developed by using a number of chemical methods, among which the metalorganic chemical vapor deposition (MOCVD) is arguably the most common for III–V compounds. Apart from homogeneous NWs, it is possible to synthesize heterostructures along the axial and radial directions, which allows for the manipulation of the NW properties and bandgap engineering.

By applying heteroepitaxy on NWs, junction geometries can also be engineered. In addition, it is easier to overcome the lattice mismatch problem when doing heteroepitaxy on bulk and/or using tensile or compressive strain, allowing more flexibility in matching the absorption to the desired wavelength. As already mentioned, NWs are 1D or quasi-1D nanostructures with unusual electronic and optoelectronic properties, arising from unique characteristics such as:

– extremely high aspect ratio: with lengths ranging from ~1 to 10 μm and diameters ranging from ~2 to 100 nm, NWs are ideal for dense device integration and exploitation of size effects, i.e. large surface-to-volume ratio and 2D quantum confinement, which lead to interesting new phenomena;

– synthetic flexibility: both top-down and bottom-up fabrication methods and growth techniques are applicable to the entire range of semiconductors, allowing us to tailor NW optical and the electronic properties through the choice of materials, doping and bandgap engineering;

– NW technologies are in principle compatible with mainstream (CMOS) fabrication processes: top-down methods include *in situ* fabrication by conventional lithographic techniques and processing, or direct transfer of fabricated NWs on a host substrate, similar to the bottom-up methods where additional functionalities may also be integrated during the synthesis through doping or the formation of axial and radial heterostructures.

Moreover, the small lateral dimensions of NWs allow extreme heteroepitaxial growth which may be important, for instance, for the integration of III–V semiconductors on silicon platforms.

1.1.5.2. *Si and GaAs nanowire field-effect transistors*

Single-electron Si NW FETs were fabricated, and a Coulomb blockade was observed even at room temperature ([SUN 11, Figure 4]). The effects of length-induced strain on the transport properties of such devices were investigated.

Gallium arsenide (GaAs) NW FETs with universal (back) gates are routinely fabricated by photolithography and electron-beam lithography on Si/SiO_2 substrates to determine NW transport parameters (Figure 1.5). Transport properties of three-branch monolithic GaAs NW junctions are being investigated for the realization of Y-junction transistors and quantum junction devices [DAI 11].

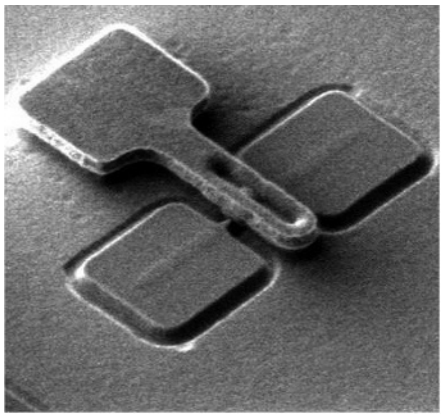

Figure 1.4. *Example of a single-electron Si NW FET realized at the CINTRA UMI*

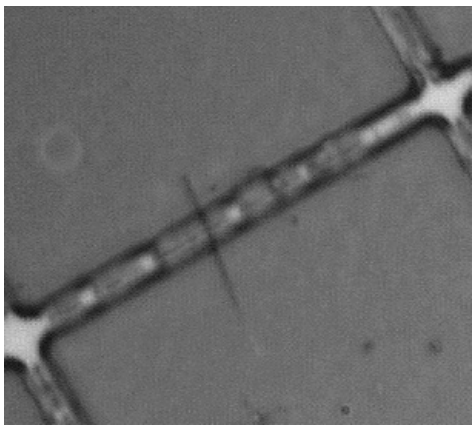

Figure 1.5. *Example of a GaAs NW FET realized at the CINTRA UMI*

NW-based FETs operating as high-sensitivity THz detectors have been realized [VIT 12] with a photovoltage signal corresponding to responsivity values >10 V/W, at 1.5 THz. The potential scalability to even higher frequencies and the technological feasibility of realizing multipixel arrays coupled with quantum cascade laser quantum cascade laser (QCL) sources make the proposed technology highly competitive for a future generation of THz detection systems.

Semiconductor NWs are an ideal building block for implementing rectifying diodes or plasma-wave detectors that could be well operated into the THz, due to their typical attofarad-order capacitance. As active channel of our FET detectors, we select indium arsenide (InAs) NWs since they show reasonably high electron mobility even at room temperature (~1000 cm²/Vs) and a potentially long electron mean free path, enabling high transconductance at very low drive voltages. InAs NWs with l.5 m length and having a diameter of 30 nm were grown bottom-up on InAs (111) B substrates by chemical beam epitaxy (CBE).

1.1.5.3. *ZnO nanorods*

In recent years, 1D semiconducting nanostructures have attracted tremendous interest for their unique physical properties attributed to their small dimensions. Driven by their enticing potential as nanoscale building blocks for integrated electronic and photonic circuits, many efforts have been devoted to the fabrication and characterization of functional devices based on 1D nanostructures, such as FETs, sensors, lasers and solar cells. In parallel, integration of device elements has been explored by both top-down and bottom-up techniques. To fully utilize the scaling advantage of the 1D structures, vertical alignment provides an efficient and flexible way to construct 3D architectures. In fact, 3D architecture using semiconducting NWs as scaffolds has been used for vertical FETs [NG 04] and field-emission devices [GAN XX]. In most of the earlier reports, vertical 1D semiconductor materials were grown on epitaxial substrates. The control of their horizontal ordering and density requires a complex process [GAN 04, MAR 03]. In addition, the resulting 1D arrays are free-standing, thus posing difficulty to fabricate “bottom” and “top” electrodes to address individual 1D channels. In this work, a high-density zinc oxide (ZnO) NW array was assembled into an anodic alumina membrane (AAM) via the CVD method assisted by electrodeposition of tin (Sn) catalysts. The electrical transport and photoconduction of individual vertical ZnO NWs were characterized using conductive atomic force microscopy (AFM). AAM has been widely used as a template for fabrication and direct assembly of a variety of 1D nanostructures [GAN 04]. Its advantage lies in the convenience of controlling the aspect ratio and the integration density.

Among the II–VI semiconductors, ZnO NWs have been extensively studied for their abundant physical properties and numerous device applications. At the material level, ZnO has a stable wurtzite crystal

structure. The zinc atoms are tetrahedrally coordinated with four oxygen atoms, which can be considered as two interpenetrating hexagonal lattices of zinc and oxygen. ZnO is a semiconductor that shows strong piezoelectric and pyroelectric properties. It has a direct wide bandgap of 3.37 eV at room temperature. As a result, ZnO nanostructures have become cutting edge nanotechnology research in transparent electronics, actuators, sensors, optoelectronics and spintronics, especially ZnO NW-based electronic devices including FETs [CHA 08].

1.1.6. *Some attempts on 0D materials*

Earlier, it was shown that quantum dots (QDs) deposited within or over GaAs can enable and/or enhance the efficiency of THz signal generation [LEY 09]. Here we describe the efficient generation of THz output signals using PC THz antennas based on semiconductor structures comprising InAs QDs embedded in high-quality crystalline GaAs, whereby the embedded QDs act as the ultrafast capture mechanism [EST 09, RAF 04].

1.2. Light/matter interactions

This section addresses the interaction between a light wave and a material aiming at the realization of new optically controlled microwave functions. This new research area, which aims towards a new family of microwave devices, deals mainly with the photoconductivity in semiconductors with 3D, 2D and 1D structures for applications ranging from the generation of microwave signals to the sampling of those signals.

Section 1.2.1 is focused on the identification of the main electromagnetic properties of specific families of matter. Section 1.2.2 discusses the mechanisms of potential optical transitions and light absorption in semiconductors and dielectric or semi-insulating material/metal interfaces. Section 1.2.3 addresses the photoconductivity of semiconductor materials.

When interacting with a material, the electric field E and the magnetic field B that define an electromagnetic wave progressing in time with a pulsation ω and a wave vector k will interact with the electromagnetic properties of the material, such as its permittivity, permeability and conductivity.

During this interaction, the coupling of these fields with the material will generate some effects on the material polarization (see Table 1.2), leading to optical signal wave vector direction modification by wave phase velocity change through optical index tuning

Material type vsPhysical effects	Refraction	Absorption	Reflection/ Diffraction
Dielectric	Electro-optic ($1^{st}/2^{nd}$ order) Acousto-optic		wave mixing
Semiconductor	Electro-absorption	Photoconductor and Photovoltaic effects	Gratings
Metal	Plasmonic	Surface or volume plasmons	Gratings

Table 1.2. *Review of main light/matter interaction*

In this book, the study is limited to two light/matter interactions occurring by absorption such as photoconductive effect and plasmonics, involving semiconducting materials and dielecric/metal interfaces properties, respectively.

1.2.1. *Fundamental electromagnetic properties of 3D bulk materials*

The distinction of semiconducting, dielectric and metallic materials originates from their electronic band structure, i.e. the spatial distribution of electrons and holes inside leading to a conductive or non-conductive behavior. The knowledge of the density of states (DoS) respecting the Fermi golden rule leads to the definition of the density of free electrons in the conduction band and free holes in the valence band. In materials demonstrating a non-zero energy gap between conduction and valence bands (semiconducting materials), highest carrier density values appear at energy levels near valence and conduction band edges such as E_v and E_c. Optical transitions by absorption and emission of energy, which can be radiative or non-radiative processes, can temporally modify these densities by generation of excitons (pairs of free carriers) according to their lifetime.

1.2.1.1. *Electronic band structure (energy band diagram and DoS)*

In 3D bulk materials, if we define the same volume denoted by *Lx, Ly* and *Lz* dimensions in the *x-, y-* and *z*-directions, respectively, equivalent to elementary $\frac{\pi}{L_x}.\frac{\pi}{L_y}.\frac{\pi}{L_z}$ volume translated in the *k*-space, then DoS expression is determined by a root mean square profile dependency with energy [ZEG XX].

DoS refers to the number of states per interval of energy at each energy level that are available to be occupied by electrons. In other words, DoS, denoted by *g(E)*, indicates how densely quantum states are packed in a particular system.

Integrating the density of the quantum states over a range of energy will produce a number of states *N(E),* equation [1.1].

$$N(E) = \int_E^{\Delta E} g(E)dE \qquad [1.1]$$

where *g(E)dE* represents the number of states between *E* and *dE.*

From the Schrödinger equation, we know that the energy of a particle is quantized and is given by equation [1.2] where *h* is Planck's constant.

$$E = \frac{k^2\hbar^2}{2m} \qquad [1.2]$$

Bearing in mind that the energy of a particle of mass *m* is given by equation [1.3]

$$E = \frac{1}{2}mv^2 = \frac{m^2v^2}{2m} = \frac{p^2}{2m} \qquad [1.3]$$

We deduce the relation, equation [1.4], between the variable *k* to the physical quantity of momentum *p*.

$$E = \frac{k^2\hbar^2}{2m} = \frac{p^2}{2m} \rightarrow k = \frac{p}{\hbar} \qquad [1.4]$$

The momentum *p* is a vector which has components in the *x-, y-,* and *z*-directions.

In a 3D system, the total energy is given by equation [1.5]

$$E = \frac{\hbar^2}{2m}\left(k_x^2 + k_y^2 + k_z^2\right) \qquad [1.5]$$

Knowing that the quantum states are separated by an interval of π/a, the volume of the unit cell (associated with a sphere) is given by equation [1.6]

$$V_0 = \left(\frac{\pi}{a}\right)^3 \qquad [1.6]$$

The DoS problem is a problem of finding the number of states in the interval of E and $E+dE$. In *k*-space, the intervals are simply k and $k+dk$. Because we are operating three dimensions, k represents the radius of a sphere in *k*-space and dk is the thickness of the sphere.

The final result for the DoS is calculated from the expression of *g(E)dE*, the number of states between *E* and *dE* (see equation [1.7]):

$$\begin{aligned} g(E)dE &= \frac{a^3}{\pi^2}\frac{2\left(2^{-1/2}\right)m^2\left(m^{-1/2}\right)E\left(E^{-1/2}\right)}{\hbar^4\hbar^{-1}}dE \\ &= \frac{a^3}{2\pi^2}\frac{2^2\left(2^{-1/2}\right)m^{3/2}}{\hbar^3}\sqrt{E}dE \end{aligned} \qquad [1.7]$$

$$g(E)dE = \frac{a^3}{2\pi^2}\left(\frac{2m}{\hbar^2}\right)^{3/2}\sqrt{E}dE$$

1.2.1.2. *Optical constants and the dielectric function + Kramers–Krönig relationships*

Kramers–Krönig relations describe the connection between the real and imaginary parts of linear complex optical functions descriptive of light–matter interaction phenomena such as susceptibility, dielectric function, refraction index and reflectivity. The real and imaginary parts are connected by a special form of the Hilbert transform. The sum rules are universal constraints that determine the results of integration over the infinite spectral range of the functions descriptive of relevant optical properties of the

medium under investigation. By applying the Kramers–Krönig relation, it is possible to acquire knowledge on dispersive phenomena by the measurement of absorptive phenomena on the whole spectrum.

Hilbert transforms connect the real and imaginary parts of a(ω) as follows (equation [1.8]):

$$\mathrm{Re}\{a(\omega)\} = \frac{1}{\pi} P \int_{-\infty}^{+\infty} \frac{\mathrm{Im}\{a(\omega\prime)\}}{\omega\prime - \omega} d\omega' \qquad [1.8]$$

$$\mathrm{Im}\{a(\omega)\} = \frac{1}{\pi} P \int_{-\infty}^{+\infty} \frac{\mathrm{Re}\{a(\omega')\}}{\omega' - \omega} d\omega'$$

Thus, the causality of $a(t)$, together with its property of being a function belonging to the space of the square-integrable functions L2, implies that its Fourier transform $a(\omega)$ is analytic in the upper complex ω-plane and that the real and imaginary parts of $a(\omega)$ are not independent but are connected by non-local, integral relations called dispersion relations.

The linear susceptibility function describes, at a fundamental level, the connection between the microscopic dynamics of the system under consideration and its linear optical properties. Nevertheless, it is experimentally much easier to measure other quantities that are more directly related to the behavior of light influenced by its interaction with matter. The most commonly used optical constants are the complex index of refraction N (ω) = η(ω) + iκ(ω), and the complex reflectivity at normal incidence r(ω). It has been shown that relevant integral relations can also be established for these quantities.

1.2.1.3. *Free carriers density*

For each type of semiconductor, extrinsic or intrinsic (i.e. doped or non-intentionally doped), at the thermodynamic equilibrium state, the concentrations of electrons n0 (9) and holes p0 (10) are defined according to the DoS in the valence band N_v and in the conduction band N_c. They depend also on the minimum energy in the conduction band Ec, the maximum energy in the valence band Ev and the Fermi level E_F. They can be expressed with respect to the intrinsic concentration n_i of the semiconductor using the action mass low (11), where T represents the temperature in Kelvin and kB represents the Boltzmann constant.

$$n_0 = N_c \exp\left[-\frac{E_c - E_F}{k_B T}\right] \quad [1.9]$$

$$p_0 = N_v \exp\left[-\frac{E_v - E_F}{k_B T}\right] \quad [1.10]$$

$$n_0 p_0 = n_i^2 \quad [1.11]$$

N_c and N_v are calculated from the product of the DoS defined in [1.7] by the Fermi–Dirac distribution function as described in the previous paragraph for 3D materials.

When the material is subjected to an external perturbation such as illumination, these carrier concentrations are modified following equations [1.12] and [1.13] and the law of mass action is no longer valid [1.14].

$$n = n_0 + \Delta n \quad [1.12]$$

$$p = p_0 + \Delta p \quad [1.13]$$

$$np \neq n_i^2 \quad [1.14]$$

The system will try to recover an equilibrium state through multiple recombinations between the free carriers in the photoexcited material. The presence of impurities modifies the structure of the material bandgap. These impurities introduce an intermediate energy level between E_v and E_c, which favors generation-recombination processes at a level called traps level.

Below, three major types of generation-recombination of electron–hole pair processes are identified.

1.2.1.3.1. Thermal (emission or absorption of phonons)

The thermal generation-recombination is linked to the emission or absorption of phonons. These thermal processes are involved in the presence of free carriers in the valence or conduction band in the frame of intrinsic or extrinsic semiconductors under equilibrium state, i.e. without optical pumping or current injection. When the temperature decreases, the thermal

generation of carriers decreases; thus, the free carrier concentration diminishes.

1.2.1.3.2. Radiative (emission or absorption of photons)

During the radiative generation-recombination, an electron–hole pair is generated or recombines through the emission or absorption of photons, respectively.

1.2.1.3.3. Auger

The Auger mechanism intervenes when a recombination between an electron and a hole followed by an energy transfer from the recombined pair to a free carrier.

In the case of the refraction of this incoming wave with a wavelength, electro- or acousto-optic interactions will modify the index of the materials and consequently to transmit the incident wave under different angles following the well-known Snell–Descartes law.

The interaction between a light wave and a material will differ according to the nature of the material [WIK]. For a conventional material ($n > 1$), the angle of refraction will be positive, and for an artificial material ($n < 0$), this angle will be negative (see Figure 1.6).

For an interaction with a completely reflecting material, the incident wave will be reflected under an angle equal to the incident wave for a conducting material. If the material is an insulator, the incident wave will be reflected or diffracted under an angle according to the Snell–Descartes law.

This chapter will be dedicated to this kind of material, especially those with a bandgap (semiconductor). A semiconductor material is an insulator that becomes a conductor under an external excitation, which could be thermal or electrical or optical. Under an external excitation, the number of free carriers for each energy band is modified. As an example, an electron in the valence band is transferred into the conduction band leaving a hole in the valence band. The energy brought by the external excitation must be greater than or equal to the gap energy in order to generate the electron–hole pairs.

The photoconductivity or photoconductive effect is based on the phenomenon of photon absorption into a semiconductor material [SAL 07].

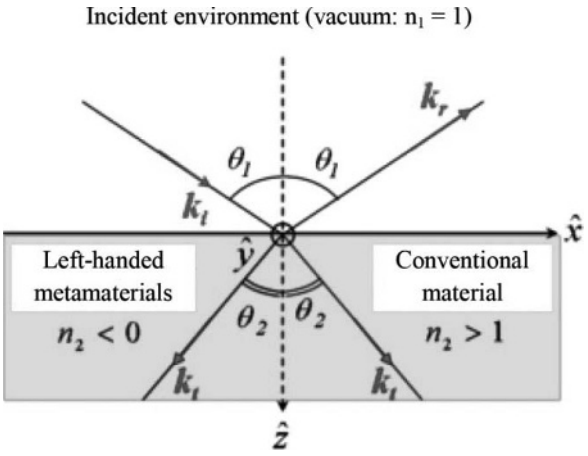

Figure 1.6. *Interaction of a light wave with a conventional material ($n \geq 1$) or an artificial material ($n < 1$). For a color version of this figure, see www.iste.co.uk/tripon/nanotechnology.zip*

Under a light illumination with an energy larger than the bandgap E_g [1.15], free carriers (either electrons or holes) are photogenerated in the material in the illuminated area.

The absorption α of the semiconductor is defined with respect to the wavelength λ of the optical signal associated with the light illumination [1.16]. In these equations, E_g is measured in eV, α is measured in cm^{-1}, h is the Planck's constant and υ is the optical frequency.

$$h\upsilon \geq E_g \qquad [1.15]$$

$$\alpha \approx 4.10^4 \sqrt{\left(h\upsilon - E_g\right)} \qquad [1.16]$$

We must therefore consider the optical wavelength/semiconductor couple in favor of the photoconductive effect (see Figure 1.7), which shows absorption coefficient for various semiconductors with respect to the photon energy and the wavelength from 200 nm to 1.4 μm. As an example, in Table 1.3, typical values for α for GaAs and Si are given.

	α (cm^{-1}) λ = 671 nm	α (cm^{-1}) λ = 800 nm
GaAs	2.6×10^4	10^4
Si	4×10^3	10^3

Table 1.3. *Absorption coefficients for GaAs and Si at two different wavelengths*

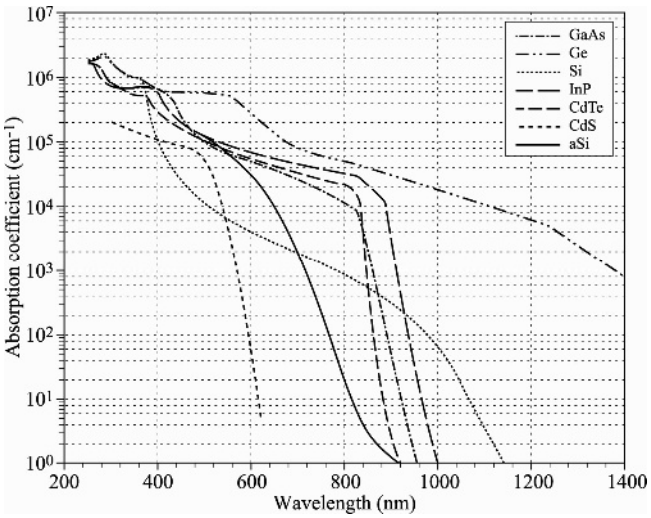

Figure 1.7. *Absorption coefficient for various semiconductors with respect to the photon energy and the wavelength from 200 nm to 1.4 μm*

During the optical illumination, the material absorbs a flux ϕ of incoming photons if the optical wavelength is included in the absorption band of the semiconductor. The expression of this flux can be determined by using the absorption coefficient α per unit of surface and time.

In the direction of the light illumination, the flux follows an exponential low decreasing proportionally to the absorption depth z and the reflection coefficient R of the surface of the semiconductor [1.16]. Its amplitude is maximum at the surface level, i.e. at $z = 0$ (equation [1.17]).

In equation [1.18], P_{opt} represents the incoming optical power and A is the illuminated area of the material, c is the speed of light and q is the charge of the electron.

$$\phi = \phi_0 \, e^{-\alpha z} \qquad [1.17]$$

$$\phi_0 = \frac{P_{opt}}{A} \frac{\lambda}{hc} \frac{1}{q} (1 - R) \qquad [1.18]$$

In the simplified case of the air/semiconductor interface, the reflectivity or reflectance r [1.19] depends on the material index $\tilde{n}_{sc}$, which in the case of an absorbing material includes an imaginary part representing the absorption [1.20].

The reflection coefficient R is equal to the square norm of the reflectance calculated at the interface [1.21] and depends on the relative permittivity of the semiconductor ε_r and on the absorption at a given wavelength λ.

$$\tilde{n}_{sc} = n - i\kappa = \sqrt{\varepsilon_r} - i\frac{\alpha\lambda}{4\pi} \qquad [1.19]$$

$$r = \frac{\tilde{n}_{sc} - 1}{\tilde{n}_{sc} + 1} \qquad [1.20]$$

$$R = rr^* = \frac{\left(\sqrt{\varepsilon_r} - 1\right)^2 + \left(\frac{\alpha\lambda}{4\pi}\right)^2}{\left(\sqrt{\varepsilon_r} + 1\right)^2 + \left(\frac{\alpha\lambda}{4\pi}\right)^2} \qquad [1.21]$$

1.2.2. *Linear optical transitions*

The optical properties of semiconductors at low light levels are often referred to as linear properties in contrast to the nonlinear optical properties. There are many physical processes that control the amount of absorption or other optical properties of a semiconductor. These processes depend on the wavelength of radiation, the specific properties of the semiconductor being studied, and other external parameters such as pressure and temperature. Optical properties of semiconductors are affected either by the introduction of impurity dopants (both *p* and *n*- type) or by unwanted impurities or

defects, similar to electrical properties. Intrinsic optical properties of semiconductors are properties that depend on their perfect crystalline nature, and extrinsic properties are brought by impurities or defects. Many types of defects exist in real solids: point defects, macroscopic structural defects, etc. Figure 1.8 schematically depicts various contributions to the absorption spectrum of a typical semiconductor as functions of wavelength (top axis) and photon energy (bottom axis). Some of the structures shown may be reduced or they are not actually present in a particular semiconductor (e.g. impurity absorption and bound excitons).

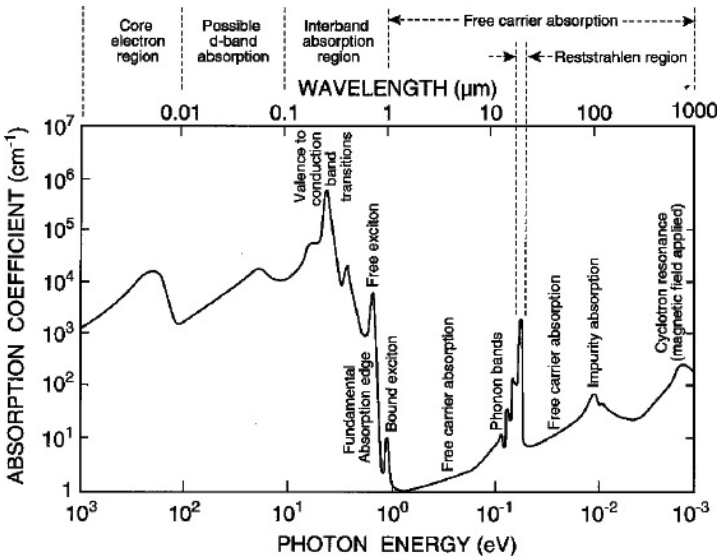

Figure 1.8. *Absorption spectrum of typical semiconductor showing a wide range of optical processes [AMI 95]*

1.2.3. *Bandgap engineering in nanomaterials: effect of confinement/sizing on bandgap structure*

1.2.3.1. *Material particularities of 2D materials: electronic band structure (energy band diagram/DoS) in 2D materials – Van Hove singularities*

In 2D, an electron is confined along one dimension but is able to travel freely in the other two directions. In the image below an electron would be confined in the *z*-direction but would travel freely in the XY plane.

In the 3D DoS analysis, a spherical volume of width *dk* had to be used. However, in 2D, the problem of calculation becomes easier because we only need to operate in two dimensions. In the 2D case, the unit cell is simply a square with a side length of π/a.

The area of the unit cell is given by equation [1.22]:

$$A_0 = \left(\frac{\pi}{a}\right)^2 \qquad [1.22]$$

Because we know the relation between k and E, we can find DoS as a function of energy.

Substituting the results into the DoS equation will give the DoS in terms of energy [1.23].

$$g(E)dE = \frac{a^2}{\pi}\left(\frac{2mE}{\hbar^2}\right)^{1/2}\left[\frac{m}{\hbar^2}\left(\frac{2mE}{\hbar^2}\right)^{-1/2}\right]dE$$

$$g(E)dE = \frac{a^2 m}{\pi\hbar^2}dE \qquad [1.23]$$

It should be noted that the 2D DoS does not depend on energy.

1.2.3.2. *Material particularities of 1D materials: energy band diagram/DoS in 1D materials*

The DoS for a 1D quantum mechanical system shows a unique solution that has application in materials such as NWs and CNTs. In both *x*- and *y*-directions, the electron is confined, but it moves freely in the *z*-direction.

Going from the 2D case to the 1D case, the unit cell becomes a line segment of length π/a.

Just as a ring was used in the 2D system to find the number of quantum states in a differential interval of energy, so a line segment is used in the 1D

situation. The line segment stretches from k to $k + dk$ or E to $E + dE$, and the length of the line is simply dE. Dividing the infinitesimal line length dE by the line length of the unit cell and then multiplying by 2 (i.e. accounting for the two electron spins), the DoS equation is [1.24]

$$g(k)dk = 2\left(\frac{L}{L_0}\right) = (2)\frac{dk}{\left(\frac{\pi}{a}\right)} = \frac{2a}{\pi}dk \qquad [1.24]$$

Replacing dE with dk, the DoS for 1D materials can be written [1.25] as

$$\begin{aligned} g(k)dk &= \frac{2a}{\pi}dk \\ g(E)dE &= \frac{2a}{\pi}\left[\frac{m}{\hbar^2}\left(\frac{2mE}{\hbar^2}\right)^{-1/2}\right]dE \\ &= \left(\frac{a}{\pi}\right)\frac{(2)2^{-1/2}(m)m^{-1/2}}{\hbar^2\hbar^{-1}}E^{-1/2}dE \end{aligned} \qquad [1.25]$$

$$g(E)dE = \left(\frac{a}{\pi}\sqrt{\frac{2m}{\hbar^2}}\right)\frac{1}{\sqrt{E}}dE$$

A typical representation of the DoS for 1D materials is shown in Figure 1.9.

1.2.3.3. *Material particularities of 0D materials: energy band diagram/DoS in 1D materials*

The DoS for a 0D structure (e.g. QD) is associated with the absence of motion and the absence of k-space to be filled with electrons. As a result, the available states only exist at discrete energies. In that case, the DoS for 0D materials can be expressed as a delta function:

$$g(E) = 2\ (E\text{-}E_c) \qquad [1.26]$$

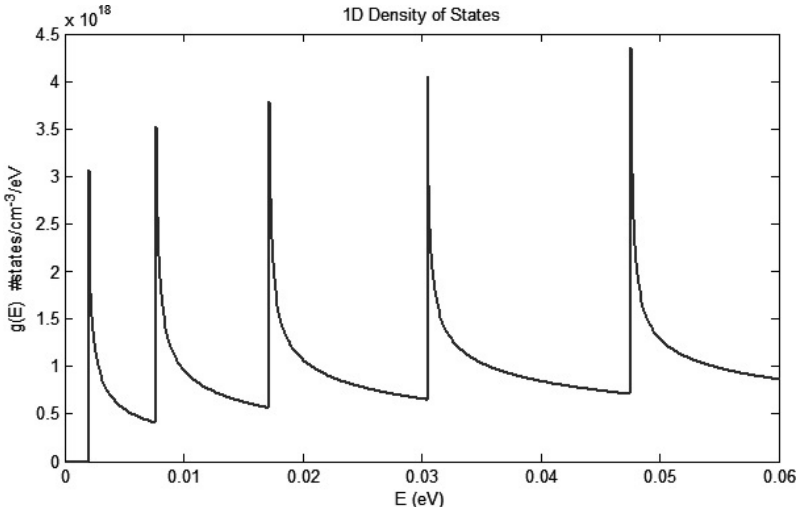

Figure 1.9. *Typical representation of the density of states of 1D materials*

1.3. Focus on two light/matter interactions at the material level

1.3.1. *Photoconductivity in semiconductor material*

1.3.1.1. *General description and some elements on the history of the field*

As an introduction, some major pioneering contributions in the field of photoconductivity have been selected.

First, we recall the work presented in 1873 by Willoughby Smith [SMI 73] who discovered photoconductivity in selenium while testing the metal for its high resistance properties in conjunction with his work involving submarine telegraph cables.

Since this early discovery, a strong effort has been made to control the speed and the efficiency of this new effect found in semiconductors

This pioneering work was followed later by a major paper by Albert Rose in 1955 [ROS 55], which concentrated on the performance of photoconductors, where he stated that "all semi-conductors and insulators are photoconductors that the characteristic parameter of a photoconductor is the lifetime of a free carrier". The photoelectron current is equal to the

product of absorbed photon current and the ratio of lifetime to transit time of a free carrier. This relation holds as well for the commonly known types of barriers as for uniform photoconductors. The photoelectron current may range from a small fraction of the photon current to many powers of 10 greater than the photon current depending on the ratio of lifetime to transit time. There is good evidence for lifetimes in different photoconductors extending from 10^{-12} s to values approaching a second. The lifetimes of free electrons and free holes are, in general, independent of each other and significantly different. Only at sufficiently high excitation rates for which the free carrier densities exceed the densities of bound states do the electron and hole lifetimes necessarily become equal. Some decades later, the time response of a photoconductor was deeply analyzed by B. Winter and E. Rosencher [ROS 98].

1.3.1.2. *Material photoconductivity*

The absorption of energy in these materials will generate localized charge carriers electron density Δn in the valence band and generation of holes density through a transfer toward the conduction band owing to their displacement in the material and the generation of a current if the material is submitted to an electric field. In this configuration, this increase of free carriers depends directly on the duration of the optical illumination and on the lifetime $\tau_{n,p}$ of the electrons/holes in the conduction/valence band before their recombination in order to reach an equilibrium state.

The intrinsic conductivity of a semiconductor material can be expressed directly as a function of the carrier density at the thermal equilibrium through equation [1.27]:

$$\sigma_0 = q\left(n_0\mu_n + p_0\mu_p\right) \qquad [1.27]$$

The photoconductivity resulting from the increase of the carrier density of the semiconductor through photon absorption is written as equations [1.28] and [1.29]:

$$\sigma = \sigma_0 + \Delta\sigma(x) \qquad [1.28]$$

$$\Delta\sigma(x) = q\left[\mu_n \Delta n(x) + \mu_p \Delta p(x)\right] \qquad [1.29]$$

The material photoconductivity is defined from the increase of the free carrier concentrations Δn(x) and Δp(x) and from the conductivity at equilibrium σ_0.

If we consider a semiconductor material located between two electrodes a length L apart and submitted to an optical illumination orthogonal to the surface length L and width W with a thickness D, the photogenerated current between these two electrodes is defined by equation [1.30] as a function of the electric field E present in the semiconductor material and the drift velocity of the electrons v_d

$$I_p = \sigma E.W.D = q\mu_n nE.W.D = qnv_d.W.D \quad [1.30]$$

As the first approximation, the generation rate of free carriers G can be written by equation [1.31], introducing the quantum efficiency η (number of generated electrons per photons), the injected optical power P_{opt} at the optical frequency ν:

$$G = \frac{\Delta n}{\tau} = \frac{\eta.P_{opt}/h\upsilon}{W.L.D} \quad [1.31]$$

The photocurrent can be defined by equation [1.32] as a function of the primary photocurrent I_{ph} in the case where the carrier lifetime is similar to the transit time of the electrons between the electrodes:

$$I_p = q.\left(\eta.\frac{P_{opt}}{h\upsilon}\right).\left(\frac{\mu_n\tau.E}{L}\right) = I_{ph}.\left(\frac{\mu_n\tau.E}{L}\right) \text{with} I_{ph} = q.\left(\eta.\frac{P_{opt}}{h\upsilon}\right) \quad [1.32]$$

The photoconductive gain is written [1.33] as the ratio of the lifetime τ and the transit time of the electrons:

$$G = \frac{\tau_t}{\tau} = \frac{\eta.P_{opt}/h\upsilon}{W.L.D} \quad [1.33]$$

The work done by Platte and B. Sauerer allowed us to approximate this spatial evolution effectively to a great extent. This equation permits us to approximate the increase of photoconductivity under optical excitation as a function of the material absorption α, the surface recombination speed of the photogenerated carriers v_s, their lifetime τ and their ambipolar diffusion length L [1.34–36]:

$$\Delta\sigma_m = \frac{\Delta\sigma_{ph}}{1+\alpha L}\left[\frac{1}{\alpha L}\left(\frac{\alpha L^2 + v_s\tau}{L + v_s\tau}\right)\right]^{\frac{-\alpha L}{1-\alpha L}} \quad [1.34]$$

$$\text{with} \quad d_e = \frac{1}{\alpha}\left[\frac{L(1+\alpha L)}{L + v_s\tau}\right]\left[\frac{1}{\alpha L}\left(\frac{\alpha L^2 + v_s\tau}{L + v_s\tau}\right)\right]^{\frac{\alpha L}{1-\alpha L}} \quad [1.35]$$

$$L = \sqrt{\frac{2k_B T}{e}\tau\left(\frac{\mu_n\mu_p}{\mu_n + \mu_p}\right)} \quad [1.36]$$

As a result, the direct representation of the photoconductive effect is a resistance R_g inversely proportional to the increase of the photogenerated conductivity G_g.

While integrating equation [1.36], it is possible to write the photoconductance G_g by considering that the current flows through a plane (yOx) following the discontinuity length L_g, i.e. along the Oz axis.

The variation of the photoconductance G_g of the photos, which is written by equation [1.37], becomes an integral along $\vec{x}$ (xx) with a uniform illumination in the (yOz) plane

$$G_g = \int \Delta\sigma(x)\frac{dS}{dz} = \int \Delta\sigma(x)\frac{dydx}{dz} \quad [1.37]$$

$$G_g = \frac{w_{eff}}{L_g}\int \Delta\sigma(x)dx \quad [1.38]$$

So when the semiconductor gap is illuminated by an optical beam at a wavelength λ, with a constant optical power P_{opt}, and a diameter w_{eff}, a photoconductance G_g (equations [1.39] and [1.40]) is generated at the level of the illuminated area A, in parallel to the capacity C_g, with a quantum efficiency η (close to 1), where R is the reflection coefficient of the substrate:

$$G_g = \frac{w_{eff}\Delta\sigma_{ph}}{L_g\left(1-\alpha^2L^2\right)}\left(\frac{1}{\alpha} - L\frac{\alpha L^2 + v_s\tau}{L + v_s\tau}\right) \quad [1.39]$$

with $$\Delta\sigma_{ph} = \frac{e\lambda}{hc}\frac{P_{opt}}{A}\left(\mu_n + \mu_p\right)\eta\alpha\tau\left(1-R\right) \quad [1.40]$$

$$R_g = \frac{1}{G_g} = \frac{L_g\left(1-\alpha^2L^2\right)}{w_{eff}\Delta\sigma_{ph}\left(\frac{1}{\alpha} - L\frac{\alpha L^2 + v_s\tau}{L + v_s\tau}\right)} \quad [1.41]$$

The constant illumination of a semiconductor material has been simulated by a resistance R_g defined by G_g equation [1.41]. This equation allows us to find the value of the generated photoresistance as a function of the intrinsic parameters of the substrate and of the illumination.

1.3.1.3. *Two-photon absorption*

Some semiconductor materials can simultaneously absorb two photons' energy equal to half the bandgap energy E_g.

This behavior is associated with materials, which have complex index κ equations [1.42] and [1.43], with a nonlinear imaginary part proportional to the light intensity I.

These materials are characterized by an two-photon absorption coefficient $\beta(\omega)$ which depends on the optical pulsation ω, on the index n, on the bandgap energy E_g of the material equation [1.44] and on the Kane's momentum P equivalent to equation [1.31] for most of the semiconductor materials.

For GaAs, the value of the coefficient $\beta(\omega)$ is equal to 5 cm/GW at λ = 1.55 μm at room temperature (T = 300 K). For LT-GaAs, $\beta(\omega)$ reaches 35 cm/GW.

$$\kappa = \kappa_0 + \beta(\omega)\frac{c}{2\pi\upsilon}I \quad [1.42]$$

with $\beta(\omega) = 724\frac{\pi}{5}\left(\frac{e}{hc}\right)^2 \frac{\hbar P}{n^2 E_g^3} \frac{\left(2\hbar\omega/E_g - 1\right)^{\frac{3}{2}}}{\left(2\hbar\omega/E_g\right)^5}$

$$P = \hbar\sqrt{\frac{10,5}{m_0}} \qquad [1.43]$$

$$\kappa_0 = \frac{\alpha\lambda}{4\pi} \qquad [1.44]$$

These materials can be optically excited at an optical wavelength λ_{2p} equal to twice the absorption wavelength λ_g corresponding to E_g. The first photon will allow an electron in the valence band to reach a superior intermediate energy level centered in the bandgap. The second photon transfers its energy to this electron, which will have access to the conduction band.

This nonlinear absorption effect in these materials opens the way to the realization of optically controlled circuit materials with a high-power optical source at a wavelength equal to $2\lambda_g$.

As an example, for GaAs, it could be interesting to use an optical source at 1.55 μm corresponding to the conventional telecommunication wavelength.

1.3.1.4. *Recent 1.55 μm semiconductor materials*

Conventional ultrahigh speed photoconductors are based on semiconductor materials such as LT GaAs sensitive to the wavelength of 0.85 μm. Widely known impulse laser diodes have been developed at 1.55 μm with high repetition rates in the few GHz range for fiber optic telecommunications. However, at 1.55 μm, the LT GaAs is no longer sensitive, and it was necessary to study semiconductor material with characteristics equivalent to LT GaAs in terms of dark resistivity and lifetime or recombination time but operating at 1.55 μm.

At the beginning of the 21st Century, numerous research activities have been developed to realize materials at 1.55 μm, such as indium gallium arsenide (InGaAs) and LT InGaAs, [MAN 07] together with the insertion of ErAs nanoparticles in InGaAs [ZHA 10].

Now the research activities are focused on:

1) ternary compounds such as GaBiAs [PAC 09];

2) quaternary compounds such as GaAsSbN [TAN 13] and GaInAsN [GRA 12];

3) two-photon absorption in GaAs photonic crystals [COM 08];

4) Fe-doped InGaAs [HAT 11];

5) Fe-doped InGaAsP [FEK 11];

6) InGaAs/InAlAs [SAR 08].

Table 1.4 presents some elements for the comparison of performances of new ultrahigh speed photoconductor operating in the 1.55 μm region.

Type of semiconductors	Response time (ps)	Dark resistivity (Ohm.cm)	Mobility ($cm^2/V.s$)
GaAsBi	1	60	2,000
GaInAsN	4.4		
GaAsSbN	1.3	1×10^7	
TPA GaAs	1		
LT-InGaAs	0.2	3	490
Fe doped InGaAs	0.6	2,200	
ErAs/InGaAs superlattice	0.2 – 0,6	340	
InGaAs/InAlAs	0.75	10^6	
Be-doped InGaAs/InAlAs multilayer	1	100–200	500– 1,500
Cold Fe-implanted InGaAsP	0.3–3	1,200 Up to 2,500	400

Table 1.4. *Comparison of performances of new photoconductor operating at 1.55 μm*

1.3.1.5. *Interest for increasing the confinement and low-dimensional materials*

Recent research involving UPMC (Paris 6 University), IEMN (CNRS and University of Lille) and Thales have shown the importance of reducing the gap dimensions in order to increase the photoconductance. As shown in Figure 1.10, when reducing the gap length Lg and the optical beam diameter, the photoconductance increases exponentially. Numerical models of photoconductivity through equation [1.26] help us to determine potential high photoconductance as a function of optical beam diameter, gap length and width dimension tunings. Also in Figure 1.10, the photoconductance Gg value is calculated as a function of optical beam diameter for different gap lengths. As a result, a reduction of gap length from 50 to 0.5 m improves photoconductance by a factor of 100 with an optical beam diameter of 62.5 µm (multimode fiber – MMF). Also, an optical beam diameter of 5 µm (single-mode fiber – SMF) enhances Gg by a factor of 10 for a gap length of 0.5 m compared with the same power illumination with an optical beam diameter of 62.5 µm. Then, an optical focusing system allows us to reduce the gap length and increase the On/Off ratio [TRI 12].

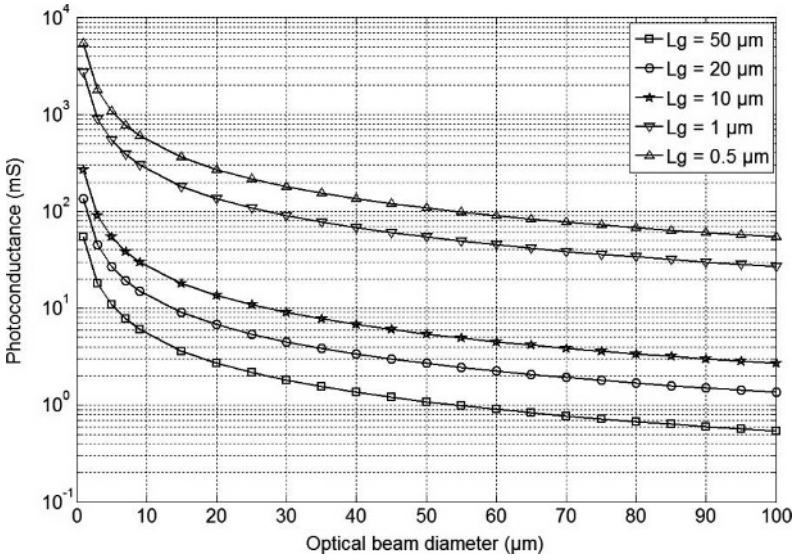

Figure 1.10. *Photoconductance as a function of optical beam diameter for various gap lengths (GaAs substrate, $\lambda = 0.8$ µm, $P_{opt} = 100$ mW, $\eta = 1$, $P = 30\%$, $\mu_n+\mu_p = 8900 cm^2/Vs$, $\alpha = 4.10^4 cm^{-1}$ $v_s = 10^4 cm/s$, $L = 2\mu m$, $\tau = 200$ ps)*

1.3.1.6. *General optical properties of SW CNTs (1D)*

CNT-based optoelectronics devices started their emergence 10 years ago because of their exceptional material optical properties in terms of band diagram, delivering direct energy band transitions and drastically reducing phonon-assisted transitions responsible for noise in global performances and low defect density, compared with classical bulk semiconducting materials. In this way, photoconductive and photovoltaic effects in SW and MW CNTs are mainly exploited to develop NIR photodetectors. Today, this material acts as a new contributor for THz signal generation by photomixing.

1.3.1.6.1. Electronic nature of SWCNTs

The electronic properties of CNT are defined from a graphene monolayer where carbon atoms are spatially distributed as a periodic honeycomb geometry (Figure 1.11). From the growth process, CNTs are formed as an axial graphene sheet rolling following a chiral vector Ct relying on two arbitrary vectors a_1 and a_2 separated by an angle ϑ as

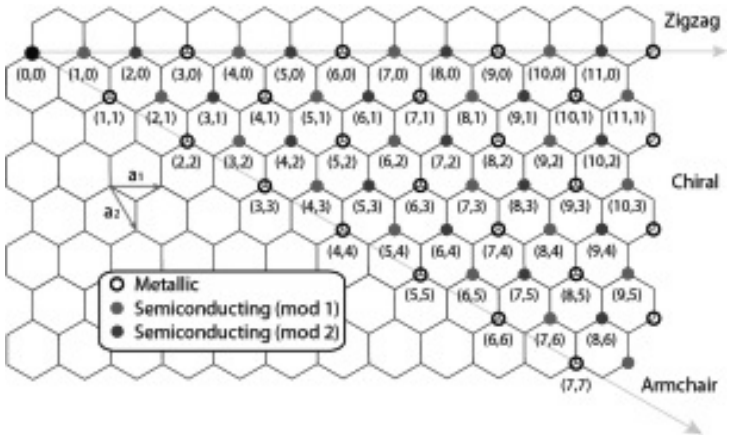

Figure 1.11. *Representation of CNT electronic nature with chirality indices (n,m). For a color version of this figure, see www.iste.co.uk/tripon/nanotechnology.zip*

$$\vec{C}_h = n\vec{a}_1 + m\vec{a}_2 \qquad [1.45]$$

$$\cos\theta = \frac{2n+m}{2\sqrt{n^2+nm+m^2}} \qquad [1.46]$$

The two *n* and *m* integers define the chirality of a CNT by imposing the direction of C_h, which can be identified as zigzag, armchair or strongly chiral.

This (n,m) integer pair also determines the CNT electronic nature as a semiconducting or metallic nanomaterial if $m = 3N$ and $n = 0$, $m = n$, $2m + n = 3N$, in a zigzag, armchair or chiral configuration, respectively, as in equations [1.45] and [1.46].

CNT diameter is also related to this (n,m) integer pair as expressed in [1.47].

$$d_t = \frac{\left|\vec{C}_h\right|}{\pi} = \frac{a_0}{\pi}\sqrt{n^2 + nm + m^2}$$

with $a_0 = \sqrt{3}.a_{C-C} = 0{,}246\ nm$ [1.47]

1.3.1.6.2. SW/MW CNT energy band diagrams

Optical absorption and emission properties of SW/MW CNTs rely on their energy band diagram characterized by unconventional conduction and valence bands profiles with discretized energy spikes values known as Van Hove singularity pairs (Figure 1.12). The energy separation between the highest valence band and the lowest conduction band singularities is given by [1.48] and [1.49], where $a_{c\text{-}c}$ is the lattice distance of two carbon atoms (~0.142 nm) and d_t is the SW CNT diameter.

$$E_{11}^{s}(d) = 2a_{c-c}\gamma_0/d_t \quad [1.48]$$

$$E_{11}^{m}(d) = 6a_{c-c}\gamma_0/d_t \quad [1.49]$$

As shown in Figure 1.12, the first Van Hove peaks determine the authorized transfer energy for both semiconductor and metallic SW CNT [MIN 01], from a global energy band diagram study. Thus, optical transitions occur at $E_{11}^{s}(d), 2E_{11}^{s}(d), E_{11}^{m}(d), 4E_{11}^{s}(d)$ .... energy levels, which are determined experimentally from fluorescence and emission spectra from photoluminescence or electroluminescence and/or absorption spectra from Raman spectroscopy. These energy levels strongly depend on the tube diameter and chirality vector.

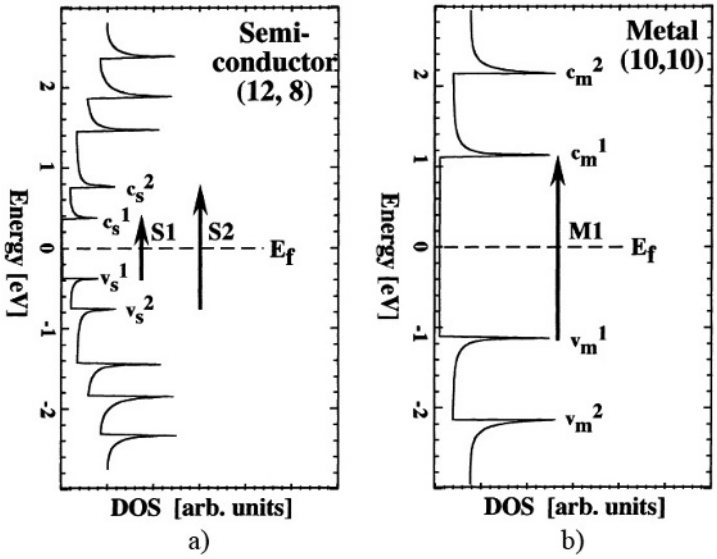

Figure 1.12. *Energy levels as a function of DoS for a) semiconducting and b) metallic SW CNT[PIE 101]*

1.3.1.6.3. Semiconducting and metallic SW CNT optical absorbance spectra

From a classical description of electron/hole pair propagating on cylindrical surface, absorption spectra can be modeled by [1.50] [PED 04]:

$$\alpha(\omega) \propto \frac{\Sigma\left|\psi_n(x,y)\right|^2}{(E_n - E_g).(E_n + E_g - \hbar\omega)^2 + (\hbar\Gamma)^2} \qquad [1.50]$$

where $\psi_n(x,y)$ is the nth exciton state with energy E_n, $\hbar\omega$ is the photon energy of light excitation, $\hbar\Gamma$ is the phenomenological line width of 0.05 eV, and $E_g = E_{exc} - E_{bind}$ is the bandgap of the CNT, where E_{bind} is the exciton binding energy and E_{exc} is the exciton energy. From this formula, absorption spectra appear as a sum of Lorentzian curves depending on the diameter of the nanotube through the E_g parameter, covering a wideband optical wavelength spectrum from UV to NIR.

For semiconducting SW CNT, two typical absorption peaks characterizing the lowest and the second interband electronic transition, referred to as S_1 and S_2 in Figure 1.13, are well identified with an energy of 0.7 eV and 1.2 eV, respectively.

Absorbance spectra can be shifted by doping, high-pressure treatment or chemical exposure [WAN 12, ZHA 06]. Also, in the case of a multilayered CNT film characterized by a specific thickness and an average nanotube diameter, absorbance optical spectra can be modified by an S1 peak shift of few meV.

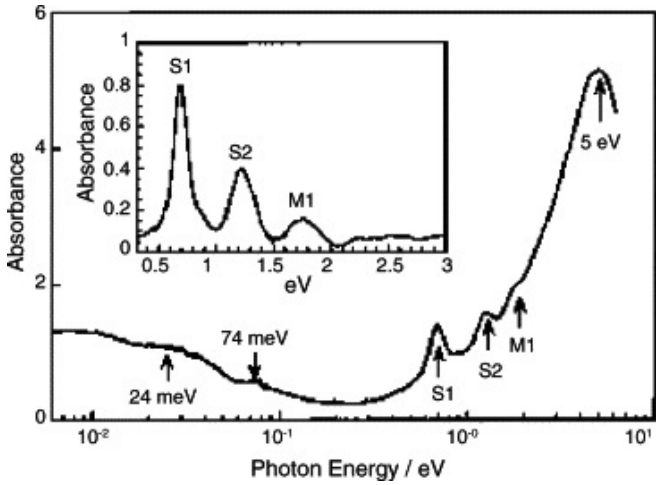

Figure 1.13. *Optical absorption spectrum of SWNT film in air at atmospheric pressure in a wide range of energy from UV to far-IR [PIE 10]*

In the framework of this project, absorbance spectra of commercial CNT are identified by the provider NanoIntegris for both semiconducting and metallic SW CNT, as shown in Figure 1.14. An absorbance of 50% at a wavelength of 0.8 µm is expected for a CNT mixture of 99% semiconducting and 1% metallic.

1.3.1.6.4. Semiconducting absorption coefficient and quantum efficiency

Absorption peaks (Van Hove singularities S11 and S22) of typical CNT types with 1-nm diameter are fairly well matched with commonly used infrared spectrum. An equivalent absorption coefficient of $24 \times 10^4 cm^{-1}$ is reported for CNT bundles, which is high compared to the absorption coefficient of LT GaAs (6,000 cm^{-1}). This point shows another potential advantage of CNTs as compared to semiconducting material [HAQ 06].

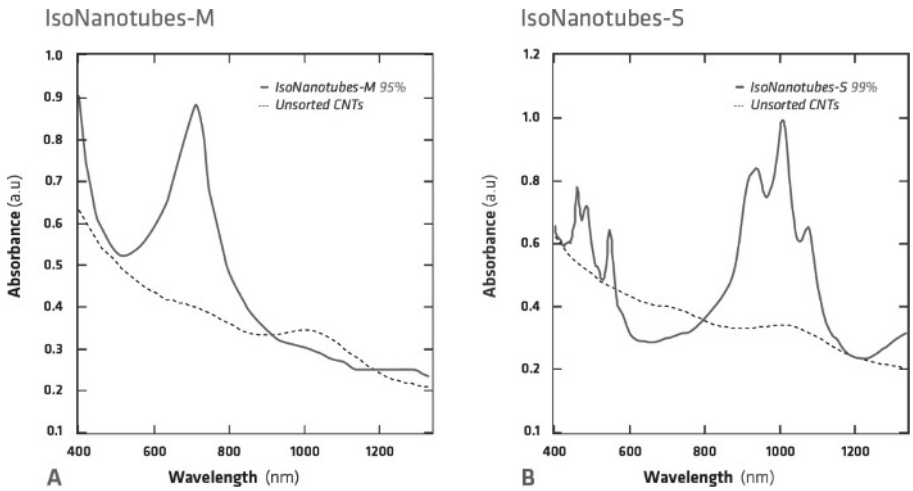

Figure 1.14. *a) Absorbance spectra of metallic and b) semiconducting SW CNT delivered by NanoIntegris*

External quantum efficiency η_e representing the percentage of photons that are able to excite electron–hole pairs depends on both the material and the test device structure. In the case of optical THz photomixing, the 10% quantum efficiency value corresponding to CNTs is lower than the 40% quantum efficiency value achieved in LT GaAs under the same experimental conditions [HES 02].

Energy transitions are dependent on tube diameter, implying an absorption coefficient wavelength dependency. Specific optical measurements such as Raman spectroscopy are necessary to check the spectral absorption band of the material (Figure 1.15).

1.3.1.6.5. Light excitation polarization dependency

Considering p and p' integer scripts for π valence and π^* conduction bands, optical transitions occur under parallel or perpendicular light polarization for a p-p' difference equal to 0 or ±1, respectively. In the last case, due to depolarization effects, transitions are suppressed leading to allowed optical transitions only under parallel polarized light. This effect has been characterized by electroluminescence in [KIN 10] and by photocurrent measurement in [QIU 05] (Figure 1.16).

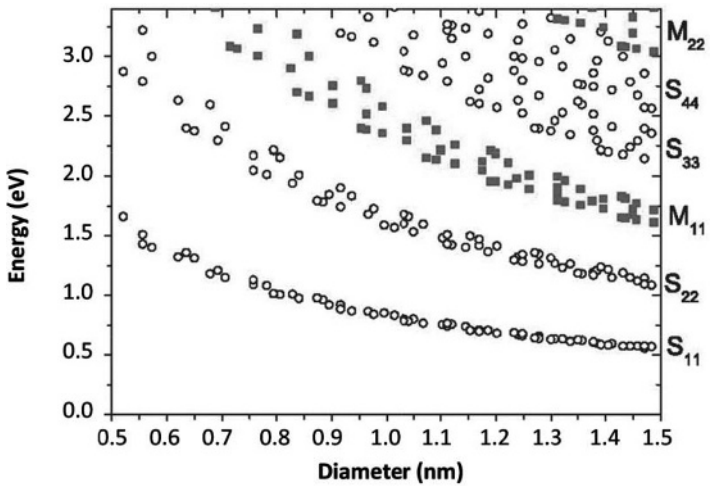

Figure 1.15. *Energy transition versus SWCNT diameter [DRE 05]*

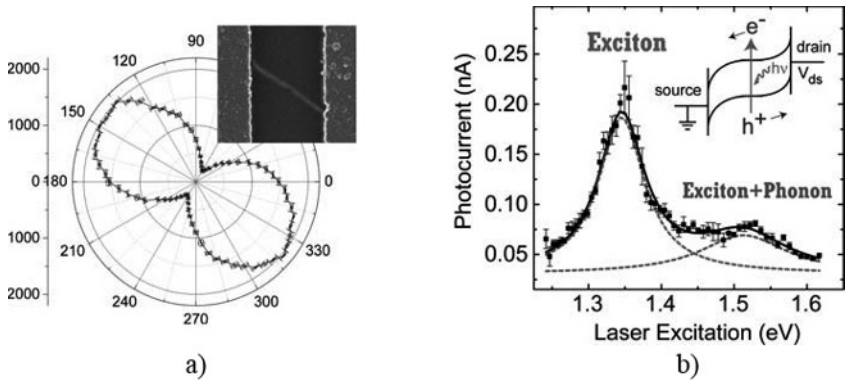

Figure 1.16. *Polarization and wavelength dependence of the photocurrent. a) Polarization dependence of the photocurrent. The photocurrent is maximized for linearly polarized light along the length of the CNT. b) Wavelength dependence of the photocurrent. The photocurrent peaks at the expected S22 exciton transition [QIU 05]*

1.3.1.7. *Metal/CNT contact-type influence*

For optoelectronic applications, metal characteristics of CNT-based devices must be studied for electrical characterization and understanding of electron and holes-generated photocurrent behavior, as in many cases a Schottky barrier is created at the CNT/metal interface. The work function of

CNT estimated to 5 eV determining this barrier height with considered metal justifies the choice of asymmetrical electrodes' access in order to avoid carrier photocurrent suppression [HON 10a, Figure 1.17]).

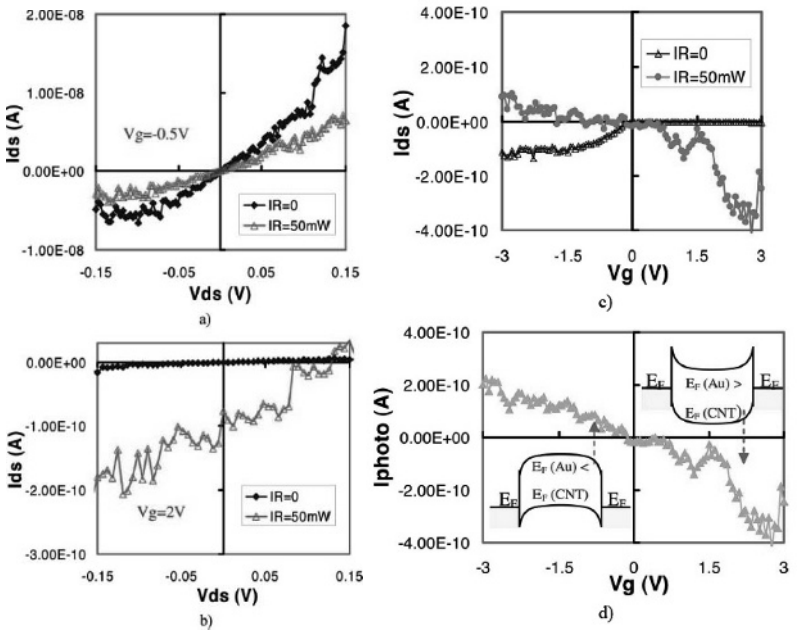

Figure 1.17. *a) Transfer characteristics of the Au-CNT-Au CNTFET with IR source OFF (IR = 0) and ON (IR = 50 mW) at zero bias. b) Relationship between gate voltage and photocurrent and corresponding band diagrams at negative and positive gate voltages – bias-dependent measurement of the Au-CNT-Au CNTFET with IR = 0 and IR = 50 mW at c) Vg = −0.5 V and d) Vg = 2 V*

1.3.1.8. *DC optoelectronic properties*

The photoconductive behavior of CNTs mainly depends on three criteria:

1) CNT orientation to electrical accesses, which enables photocurrent measurement under bias or in a bias-free configuration. For this criterion, CNT deposition method will;

2) CNT density, which also determines the contact resistance value with electrodes' metallization;

3) CNT contact type with electrical accesses metal which can rapidly establish a different Schottky barrier for electrons and holes leading to a potential photocurrent annealing as in CNT-based infrared photodetection [HON 10b].

From DC electrical characterization, the key parameter extraction such as photoconductance can be achieved by photocurrent measurement, assuming the active area volume is determined in two identified configurations as follows:

– Planar unique or bundles of CNT: in this case, the active area volume V is estimated by the product of the surface of a CNT (L_{CNT} x $2\pi d_{CNT}/2$) with a thickness equal to an atomic layer and with the number of CNTs;

– Vertical CNT bundles (N × M CNTs): in this case, the active area volume V is estimated by the product of the active surface of a CNT (de × 2πdCNT/2) with a thickness equal to an atomic layer and with N × M.

1.3.1.8.1. State of the art for horizontal unique SW CNT case

In the case of CNTs deposited in the same plane as electrical access, the benefit of CNT-based electronic devices such as p-n junctions and FETs electrical characterization under specific illumination is crucial.

In the case of p-n junctions, illumination absorption can be transferred on a unique CNT through two processes: first, the excitation of one electron from valence band to conduction band by the absorption of a photon with energy larger than the bandgap and, second, a photon-assisted tunneling process when the photon energy is less than the bandgap. Calculation of the generated photocurrent as a function of the incoming photon energy leads to a spectral photoresponse characterized by multiple peak values due to the multiple direct bandgaps.

For both types of CNT-based electronic devices, I–V characteristics have demonstrated a change in current under bias on one (p-n junction) or two contacts (FET) associated with IR illumination, as shown in Figure 1.18 from [FRE 03] considering a CNT-FET and in Figure 1.19 from [GUO 06] considering metallic and semiconducting CNT-SBFET.

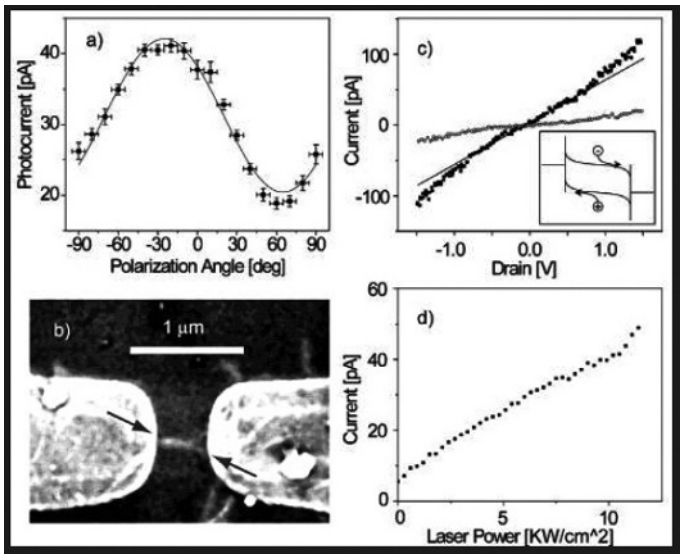

Figure 1.18. *a) Photocurrent as a function of the polarization angle of the incident infrared light. (Excitation energy 1.28 eV, drain voltage +1 V and gate voltage −1.5 V.) b) SEM image of the NTFET. The maximum current in c) is observed with light polarized along the nanotube axis (indicated by the arrows). d) Drain-voltage dependence of the current (O) without light and with infrared light [GUO 06]. (Gate voltage, −2 V; IR intensity, 5.6 KW/cm^2) [FRE 03]*

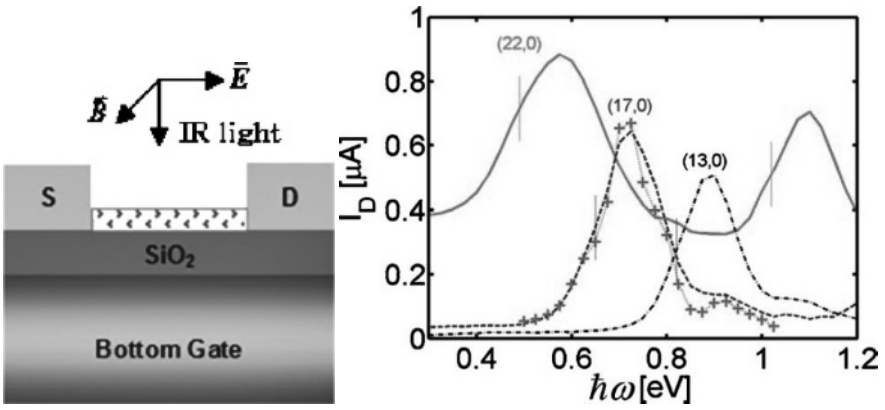

Figure 1.19. *The source-drain current versus the photon energy for a (22,0) CNT with $E_g \approx 0.49$ eV (the solid line), a (17,0) CNT with $E_g \approx 0.63$ eV (dashed line) and a (13,0) CNT with $E_g \approx 0.82$ eV (dashed-dotted line) under the illumination intensity of 107 W/cm^2 at VG = VD/2 = 0.2 V in the presence of electron–phonon coupling. For comparison, the dotted line with crosses shows the current of the (17,0) CNT without electron–phonon coupling. The vertical bars show the subbandgap*

1.3.1.8.2. State of the art for SW CNT film case

For a film constituted of planar CNTs array, photocurrent measurements have been performed by using a two-electrode device underneath the film allowing bias of the structure [LIU 09]. In this example, the photoconductivity showed an increase, decrease or even negative values when the laser spot was on different positions between contact electrodes, showing a position-dependent photoconductivity of partially aligned films of CNTs. Photon-induced charge carrier generation in SWCNTs and subsequent charge separation across the metal–CNT contacts are believed to cause the photoconductivity changes.

A net photovoltage of 4 mV and a photocurrent of 10 μA were produced under the laser intensity of 27 mW with a quantum efficiency of 7.8% in vacuum (Figure 1.20). The photocurrent was observed to be in the direction of nanotube alignment. Finally, it was found that a strong dependence of the polarization of the incident light on the photocurrent and the orientation of the films influenced the dynamics of the rise and fall of the photocurrent.

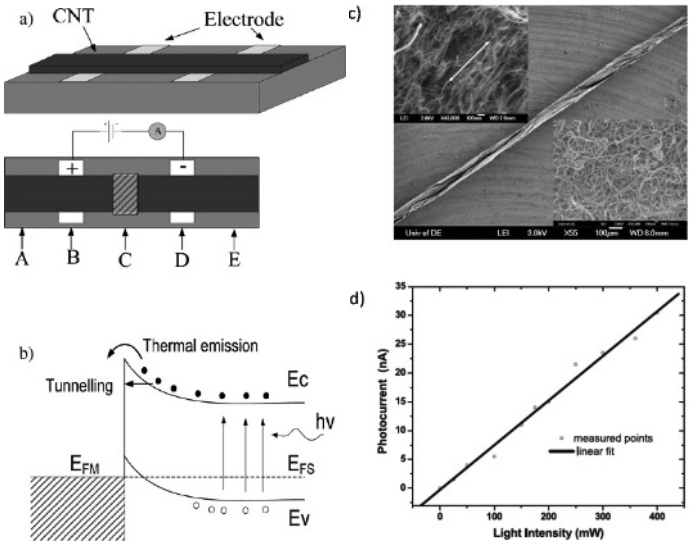

Figure 1.20. *a) Schematic of the carbon nanotube sheets under testing. The bottom part shows the top view of the device. A–E are five testing positions on the sample where a laser spot was pointed. The shaded area indicates that the laser spot was on position C. b) Band diagram of carbon nanotube (right) in contact with platinum electrodes (left). c) SEM image of a partially rolled thin film of carbon nanotubes; inset compares the non-oriented (bottom) and partially oriented (top) samples. d) The amplitude of photocurrent as a function of laser intensity. Measurements were done in an open environment*

1.3.1.8.3. State of the art for MW CNT bundle case

Through experimental comparison, it was found that macroscale CNT materials also have potential distinct optical properties. Photoresponse in bundles of MWNTs was observed by Wei *et al*. [WEI 06], Passacantando *et al*. [PAS 08] and Coscia *et al*. [COS 09]. A recent study has also shown that a MWNT film is capable of generating a position-dependent photocurrent [SUN 08, STO 08]. Photoresponse of MWNT/polymer composite films [STO 08] and photoconductivity of doped nanotubes [JIJ 06] have been studied. There were very few studies about vertically aligned MWNTs before [ZHA 10]. In this last study, length dependency on detected photocurrent level was demonstrated, leading to an estimation of the penetration depth of light larger than 300 µm in this orientation (Figure 1.21).

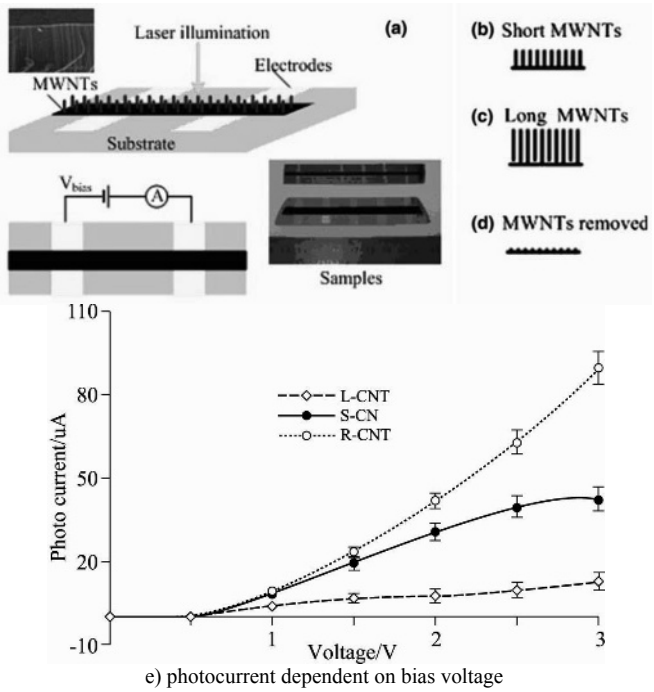

e) photocurrent dependent on bias voltage

Figure 1.21. *a) Schematic of the MWNTs device under testing. The bottom part shows the top view of the device. The electrodes are Mo; the applied voltage on the electrodes is the bias voltage, Vbias; b) short-aligned MWNTs device (20 µm length); c) long-aligned MWNTs (300 µm length); d) MWNTs removed device; e) photocurrent dependent on bias voltage at room temperature, setting laser power of 27 mW and wavelength at 532 nm. L-CNT means long-aligned MWNTs device, S-CNT means short-aligned MWNTs, R-CNT means MWNTs removed device*

1.3.1.8.4. Carrier dynamics extraction

The key parameters of carriers such as lifetime and mobility are determinant of the estimation of transient photoconductivity σ_{ph} calculated from the sum of electrons and holes conductivity σ_n from [1.51] and [1.52], considering the photogenerated electron *n* and the hole density p:

$$\sigma_n = qen\mu_n \quad [1.51]$$

$$\sigma_p = qen\mu_p \quad [1.52]$$

Photoconductance value is calculated by integration of σ_{ph} over a time corresponding to the carrier lifetime in an active volume.

A real-time investigation of ultra-fast carrier dynamics in SWCNT bundles using femtosecond time-resolved photoelectron spectroscopy has been developed and applied to identify carrier lifetimes value in CNTs bundles [HER 02]. A pump–probe scheme allows an investigation of charge carriers from 2.38 eV above E_F to the immediate vicinity of the Fermi level and below, down to about −0.2 eV, and the study of fundamental scattering processes such as e–e or e–ph scattering directly in the time domain (Figure 1.21).

A carrier lifetime of 1–3 ps with a mobility of 10^4 cm²/V.s has been obtained experimentally [HES 02] (Figure 1.22).

1.3.2. *Example of light absorption in metals: plasmonics*

1.3.2.1. *Elements on the index and phase conditions for a conventional metal/dielectric interface*

We consider the generation of surface plasmons (oscillation of electrons at a frequency defined as the plasma frequency) at the metal/dielectric interface. These surface plasmons are excited by an electric field incoming in the incident plane of the excitation (typically an optical excitation in tranverse electro magnetic (TEM) mode) and following a specific angle.

Under these conditions, the light wave incoming on the metal/dielectric interface (Figure 1.23) will be partially or totally absorbed. In this configuration, no reflection of this light wave is obtained. The reflection spectrum at the metal/dielectric interface as a function of the incidence angle will reach a minimum value at an angle of incidence called SPR angle, θ_c.

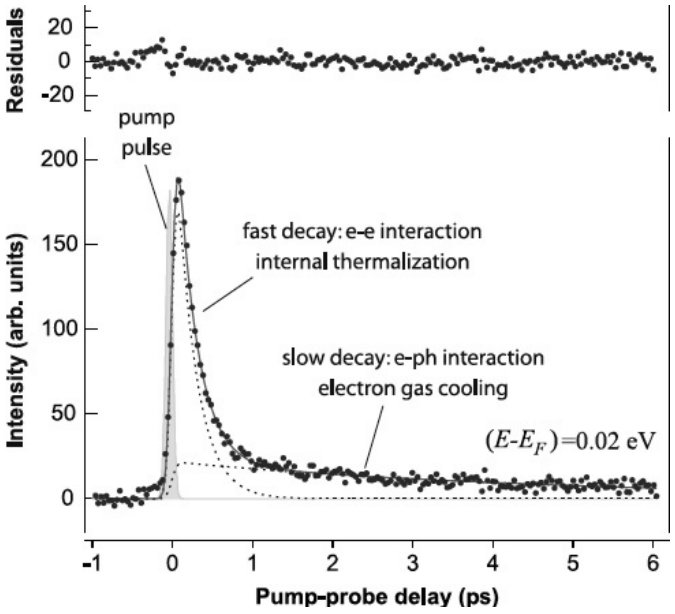

Figure 1.22. *Sample fit of a low-energy cross-correlation (XC) trace to a bi-exponential decay. The slow and fast components can be associated with e–e and e–ph interactions, i.e. internal thermalization and cooling of the electron gas, respectively*

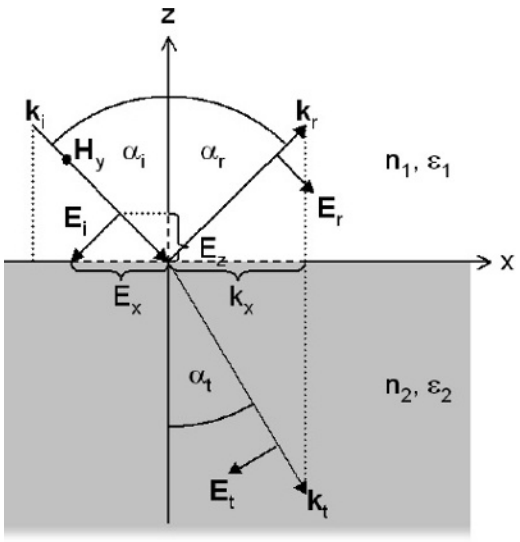

Figure 1.23. *Definition of a metal/dielectric*

The angle θ_c [1.53] corresponds to the total reflection angle defined by the index ratios n_m and n_d of the metal and dielectric material, respectively, forming the interface allowing the evanescent mode at the level of the interface and parallel to the *x*-axis

$$\theta_c = \sin^{-1}\left(\frac{n_m}{n_d}\right) \qquad [1.53]$$

Taking into account the permittivity of the dielectric ε_d, the oscillation frequency of the SPP ω_{sp} intervenes at a frequency lower than the plasma frequency ω_p [1.54]:

$$\omega_{sp} = \frac{\omega_p}{\sqrt{1+\varepsilon_d}} \qquad \omega_p = \sqrt{\frac{ne^2}{m\varepsilon_0}} \qquad [1.54]$$

It has been demonstrated that the component of the wave vector along the *x*-axis is defined by the following equation, representing the plasmonic dispersion equation [1.55]:

$$\boxed{k_x = \frac{\omega_0}{c}\sqrt{\frac{\varepsilon_d\varepsilon_m}{\varepsilon_d+\varepsilon_m}}} \qquad [1.55]$$

This dispersion equation, shown in Figures 1.24 and 1.25, allows us to understand that an optical coupling is needed in order to match the wave vector of the incident photon ($k_{photon,air}$ curve) with a plasmon present at the interface level of two dielectric materials with different optical index values (red and green curves).

A coupling via a prism or a grating (see Figure 1.26) adding a phase element in sin θ_r (θ_r representing the incidence angle in the prism or at the coupling grating level) is realized by natural reflection in the case of the prism and by disordered diffraction in the case of a periodic grating with a step Λ.

By considering the complex permittivity [1.56] of the metal:

$$\varepsilon_m = \varepsilon_m' + j\varepsilon_m'' \qquad [1.56]$$

Three conditions must be respected between this permittivity and the dielectric one:

$$\varepsilon_m' < 0$$

$$\left|\varepsilon_m'\right| \geq \varepsilon_d$$

$$\varepsilon_m'' \to 0$$

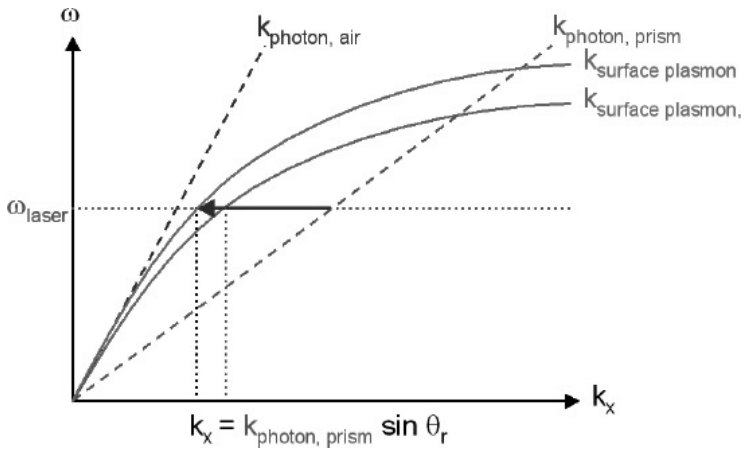

Figure 1.24. *Plasmonic dispersion relation for a prism coupling*

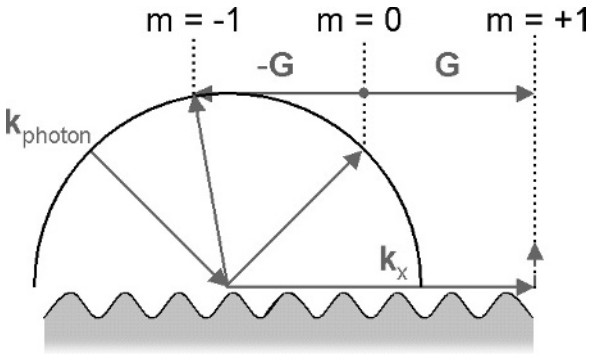

Figure 1.25. *Representation of a diffraction grating*

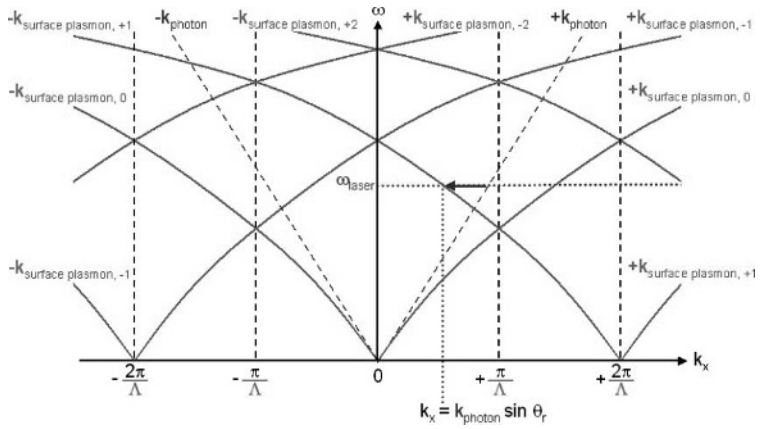

Figure 1.26. *Plasmonic dispersion relation in case of a coupling by grating*

1.3.2.2. *Matching conditions: metal/semiconductor interface*

In the conventional case, the generation of plasmon is done simultaneously between the two faces of the metal, i.e. at the coupling material/metal interface and the metal/dielectric interface inducing two potential configurations for the optical coupling either by the front face or by the rear face [KRE 71, OTT 68].

If the dielectric material is replaced by a semiconductor material for integration or efficiency reasons, a plasmon generation at the metal–semiconductor interface must be favored.

To satisfy this latest condition, constraints on materials must be taken into account. For example, it will be necessary to have an index of the coupling material greater than or equal to the semiconductor material index toward the desired incidence angle:

$\varepsilon_{prism} >= \varepsilon_{dielectric}$